scientific reports

OPEN

Epsilon negative dynamic coded THz metamaterial beamformer for digital information encryption

Eistiak Ahamed✉, Rasool Keshavarz & Negin Shariati

Light propagation facilitates digital information encryption by utilizing Epsilon Negative (ENG) metamaterials as a medium. Achieving the desired encryption hinges on synchronizing two pivotal features: the phase difference and the epsilon shifting of the metamaterials. The proposed metamaterial is intricately designed to represent digital bit 1 (states 0 and 1), contingent upon the arrangement of material multilayers within the metamaterial device. Specifically, state 1 is fashioned through a combination of Graphene and Gold, while state 0 is solely represented by Graphene on a metamaterial structure. The developed structure exhibits right hand metamaterial (epsilon of $+$ 7.20) for state 0 and plasma metamaterial (epsilon -6.94) for state 1 at 8.6 THz. Notably, the phase difference between 0 and 1 states is around $90°$. Primarily leveraging the synchronized combination phase and epsilon as the key design parameters for the metamaterial array, the beamforming pattern enables beam steering within the angular range of $+30°$ to $-30°$. Secondly, employing a sophisticated material addition strategy involving Gallium Arsenide (GaAs) systematically manipulates the sidelobe in specific directions, thereby providing a mechanism to modulate the sidelobe and concurrently augment spatial resolution. After preparing the metamaterial coded (MC) lens, the source, lens and receiver strategically encrypt the scanning image, employing techniques including Doppler compression and 2D discrete Fourier transform. The proposed MC lens offers applicability like image encryption, security scanning, conveyor systems, hyperlenses and modern cryptography.

Keywords Beamforming, Coded metamaterial, Epsilon negative, Digital information encryption, Multilayer metamaterial, Plasma metamaterial

The deployment of Terahertz (THz) beamforming has attracted tremendous attraction in recent years among researchers aiming to enhance the speed and intelligence of highly capable devices. In the realm of advanced wireless communication systems, THz technology[1] emerges as a promising solution to handle imminent challenges, notably spectrum scarcity and intricate security issues, within the dynamic environment of evolving 6G networks[2–5]. The potential of THz is intricately linked to the abundant spectral resources available in the THz band, encompassing high-penetration propagation functionalities spanning an expansive spectrum from 0.1 to 10 THz[6]. However, harnessing this potential requires a comprehensive understanding of the intricate technical nuances, complex regulatory frameworks, and ongoing interplay of emerging innovations at the forefront of wireless and THz technology research[7–9].

Metamaterials possess a distinctive functionality for effectively representing coded metamaterials[10–12]. Traditionally, the construction of metamaterial and antenna beamforming lenses relies on introducing phase shifts among predefined elements, making them applicable for various applications[13–19]. However, the specificity of this functionality enables the intricate creation of beam steering within the lens. The argumentation of negative and near zero permittivity characteristics, coupled with the capacity for phase shift, introduces the potential to elevate the metamaterial into a 'super lens'[20,21], thereby conferring an extraordinary capability for the precise extraction of information through encryption. Giovampaola et al. pioneered a digital coded metamaterial bits methodology, wherein bit states are intricately defined by permittivity functions within the near-ultraviolet frequency band[22]. The developed methodology undergoes analytical explication across a diverse scenario, encompassing digital hyperlenses and the digital epsilon near zero super coupling phenomenon. Wavelength intricacies remain unaddressed in this study within the near-ultraviolet frequency band, deliberately omitting considerations of the phase phenomena in the bit-defining process of the design methodology.

RF and Communication Technologies (RFCT) Research Laboratory, School of Electrical and Data Engineering, Faculty of Engineering and Information Technology, University of Technology Sydney, Broadway, Ultimo, NSW 2007, Australia. ✉email: eistiak.ahamed@student.uts.edu.au
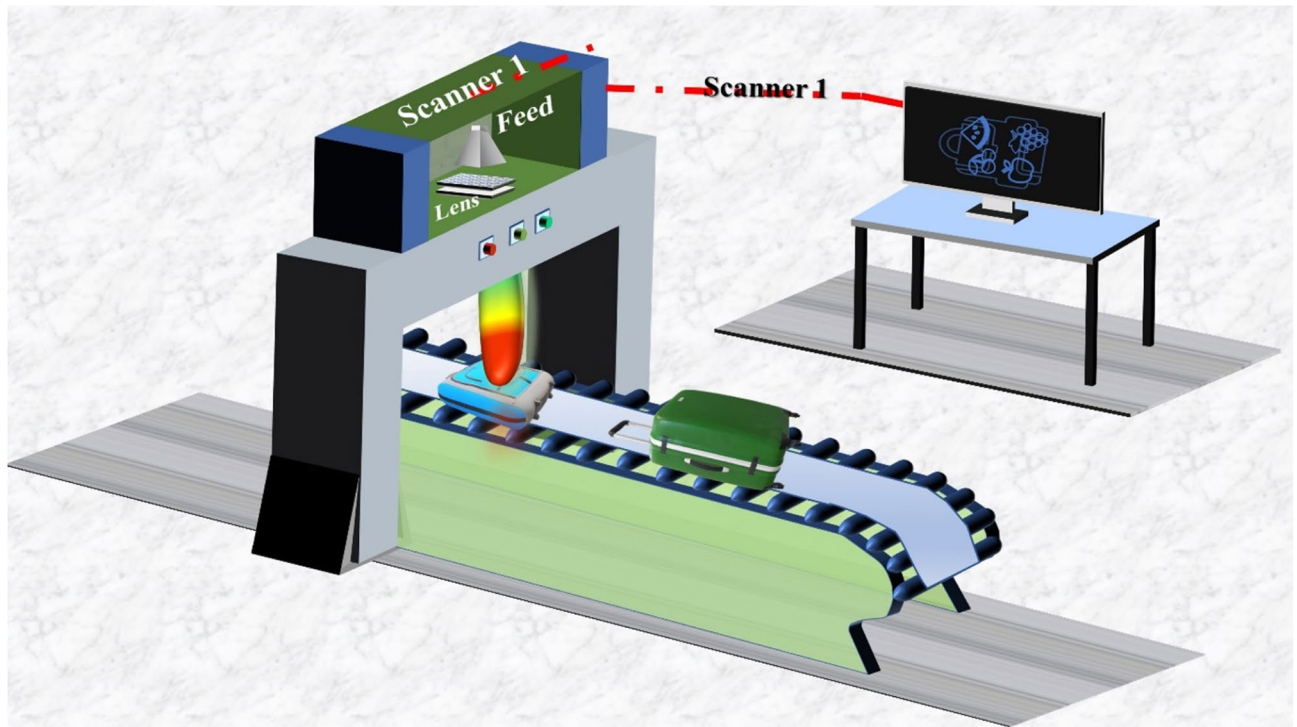
Fig. 1. Application scenario for dynamic THz metamaterial.

Liu et al. presented an Sb_2S_3 phase change metasurface capable of encoding information and generating grayscale images in near and far field orientations[23]. The ingeniously designed coded meta-atom, responsive to incident polarization, not only enables precise manipulation of phase and amplitude but also exhibits intriguing negative functionalities, most notably a negative refractive index. This paradigm-shifting metamaterial design promises to advance the frontier of metamaterial capabilities. Besides, Liang et al. designed a 1-bit arbitrary coded metamaterial for wideband applications ranging from 0.8 to 1.4 THz[24]. By employing a sophisticated methodology, the developed metamaterial governs low reflection within a specific direction spanning $0°$ to $40°$, intricately steering beams across multiple frequency ranges. Suzuki et al. developed a metamaterial with a sophisticated negative refractive index boasting values of $-2.81 + j0.049$ at 2 THz[25]. The proposed method opens avenues for superlens applications, marking a significant stride in metamaterial engineering. On another dimension of metamaterial invention, Lui et al. proposed a 1-bit LC-based multibeam transmissive metamaterial tailored for THz applications, with an additional emphasis on its applicability in the domain of imaging[26]. The carefully orchestrated array, strategically designed to mitigate radiative loss, not only markedly increased the phase tunning rate but also, in alignment with the coding pattern, yielded impressive beam steering angles of up to $30°$.

In this paper, a novel design method is employed to model a coded metamaterial characterized by its negative permittivity and phase difference properties. The designed coded metamerial exhibits the capability to transition its coded bit states between negative and positive permittivity, concurrently maintaining a consistent $90°$ phase difference for the two states. The developed MC lens, which has the unique ability to encrypt images in specific directions, holds promise for application in image processing and modern cryptography. Its multifaceted design, integrating phase-epsilon synchronization and advanced material manipulation, positions it as an advanced platform for addressing the intricacies of modern security, information paradigms, hyper and super-coupling lenses. In addition to its encryption capabilities, integrating the MC lens into conveyor systems mitigates health risks and augments image scanning depth and resolution, offering a comprehensive and nuanced analysis of scanned objects. Furthermore, by providing enhanced clarity and detail in scanned images, the lens elevates the efficiency of security protocols while minimizing environmental impact. Figure 1 demonstrates the system's dual functionality as both transmitter and receiver underscore its adaptability, rendering it instrumental in scanning consumable items, as denoted by Scanner 1. Comparatively, the proposed MC encryption system exhibits advantages over traditional X-ray systems by eliminating ionizing radiation and reducing associated health risks for edible items. Unlike X-ray systems, which require a special disposal process due to ionized radiation, the MC lens system poses minimal environmental concerns, making it a safer and more environmentally friendly option for security scanning applications.

Working mechanism

The proposed coded metamaterial, denoted as $\varnothing_1$ and $\varnothing_2$ is capable of representing the 1-bit states 0 and 1, respectively, as depicted in Fig. 2. The characteristics of the $\varnothing_1$ and $\varnothing_2$ metamaterial unit cells adhere
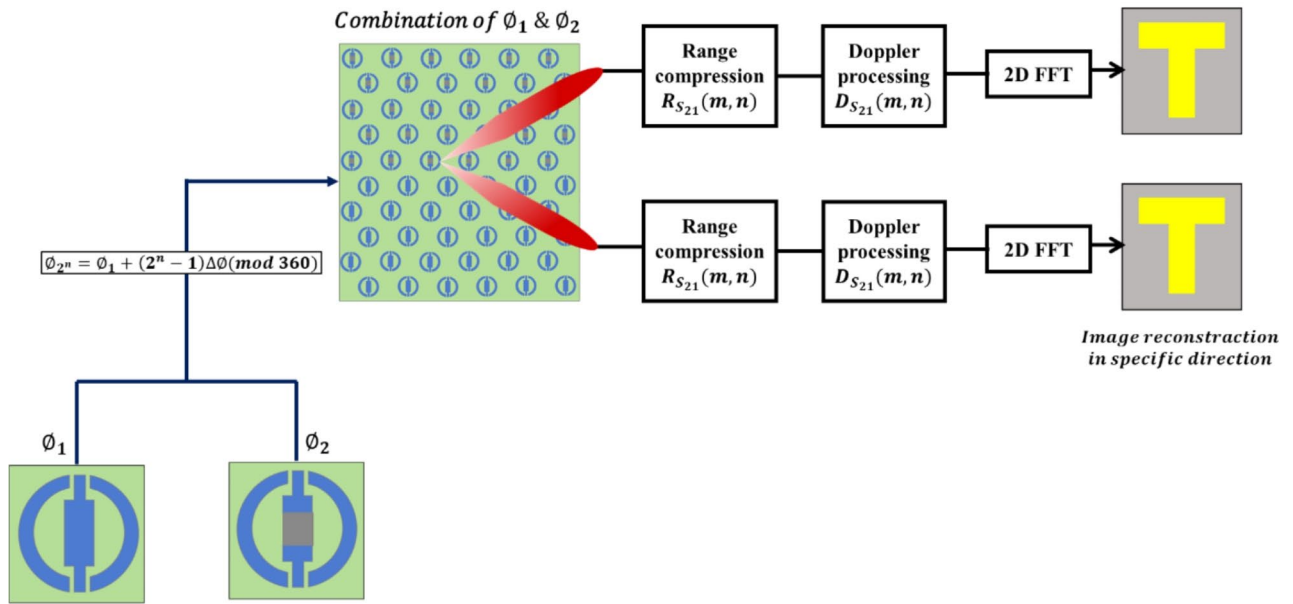
Fig. 2. The proposed coded metamaterial mechanism to extract image in a specific direction.

to the phase distribution condition $\varnothing_{2^n} = \varnothing_1 + (2^n - 1)\Delta \varnothing \ (mod 360)$, resulting in a $90°$ phase difference between $\varnothing_1$ and $\varnothing_2$. Two combinations of coded metamaterial, incorporating $\varnothing_1$ and $\varnothing_2$, are created for beamforming at $+30°$ and $-30°$ directions, adding a layer of sophistication to the designed structure. The application of the specifically directed beam extends to the scanning of objects requiring encryption.

Beam steering mechanism based on phase and epsilon difference

The interaction between phase difference and epsilon shifting plays a crucial role in achieving precise control over beam deflection and wavefront manipulation. The electric field distribution is governed by the phase difference across the metamaterial surface and the permittivity profile, which modulates the wave propagation speed. In a multilayered structure, not only does the phase difference affect energy steering, but the effective medium ratio also plays a critical role in controlling the phase to direct energy in a specific direction. The integration of materials like graphene and GaAs into the multilayer system introduces tunable epsilon shifting capabilities, contributing to phase modulation and impedance matching. GaAs, in particular, exhibits near-zero epsilon properties, which allow for improved control over phase distribution, leading to more efficient beam steering. The enhanced beam steering performance is attributed to the interaction between phase discontinuities and epsilon shifting within the multilayered configuration, as demonstrated by the 90° phase shift between modulation states. The combined effect of phase difference and epsilon shifting governs the behavior of the electric field and wavefront deflection in multiple directions. The spatial variation of permittivity, $\epsilon(x)$, along with the discrete phase difference between coded states $\varnothing_1$ and $\varnothing_2$, provides fine control over both beam steering and the encryption process.

Consider a dipole antenna placed in front of the metamaterial at a distance of r, where $r_x = x_x \widehat{x} + y_x \widehat{y} + z_x \widehat{z}$, where $\mathcal{L}(r_x \epsilon V)$ operator represents the material interaction with wavefront based on permittivity $\epsilon(x)$. The electric dipole moment is defined with $P = |P| \widehat{P_i}$, where $|P|$ is the modulus of dipole moment and $\widehat{P_i} = \widehat{P_i} e^{j\varnothing_i}$ is the complex polarization vector, where $\varnothing_i$ is the incident phase of each unit cell. The generated e-field $E(r_x)$ in metamaterial can be expressed as[1]

$$E(r_x) = \mathcal{L}(r_x \epsilon V) E_i(r_x; \widehat{P_i}) - \int_{\partial V} \left[-j\omega \epsilon_0 (\widehat{n}_0 \times \frac{-\nabla_{r'} \times E_{\partial V}(r')}{j\omega \mu_0} G_{pd}(r_x, r') \right.$$
$$\left. + (\widehat{n}_0 \cdot E_{\partial V}(r')) \nabla_{r'} G_{pd}(r_x, r') + (\widehat{n}_0 \times E_{\partial V}(r')) \times \nabla_{r'} G_{pd}(r_x, r') \right] dr' \qquad (1)$$

Where modified Green functions induced by the discrete phase difference[27]

$$G_{pd}(r_x, r') = G(r_x, r') e^{j\nabla \varnothing} \qquad (2)$$

The phase difference is defined as $\nabla \varnothing = \varnothing_2 - \varnothing_1$.

Maintaining beam alignment in a fixed direction is critical to ensure consistent image encryption. Any misalignment can lead to improper scanning, compromising the system's accuracy. The imposed phase difference is essential for stabilizing the beam, allowing precise control over the direction in which electromagnetic energy is focused, ensuring that the beam remains aligned with its intended trajectory. Furthermore, phase modulation

through epsilon shifting enhances the system's ability to dynamically track image details during scanning, facilitating the encryption of high-quality information. Electromagnetic waves exhibit unique behaviors in metamaterials with negative permittivity, such as reverse wave propagation, which generates highly focused wavefronts. This results in higher-resolution scanning, allowing the system to capture finer image features with greater precision. Modulating the encryption process through epsilon shifting provides an effective mechanism for precise control when combined with a specific phase difference. The phase difference stabilizes the incident beam angle, while epsilon shifting enhances wavefront resolution, enabling accurate scanning and encoding of each pixel in a dynamic image. At any given moment, the system accounts for the spatial encoding of the reflected beam, ensuring that null values and encoding locations are accurately tracked as the image progresses across the beam. This ensures that the final encrypted image retains high fidelity to the original pixel distribution.

The generalized beam deflection angle calculation by using phase difference and epsilon shifting is as follows, where $\theta_{pd\epsilon}$ contain both phase difference and epsilon shifting, d is the unit cell spacing in the metamaterial array and λ_0 is the free space wavelength at 8.6 THz.

$$\theta_{pd\epsilon} = arcsin\left(\frac{\lambda_0}{2\pi}\frac{1}{\sqrt{\epsilon(x)}}\frac{\nabla\varnothing}{d}\right) \tag{3}$$

The system response to scanning objects in a specific direction generates a matrix wherein the vector elements undergo normalization. The actual scanning data, denoted as V_{S21} can be normalized by multiplying it with an area scaling factor α

$$\alpha = \begin{bmatrix} \alpha_{11} & \cdots & \alpha_{(1,N)} \\ \vdots & \ddots & \vdots \\ \alpha_{(N,1)} & \cdots & \alpha_{(N,N)} \end{bmatrix} \tag{4}$$

The resultant matrix A is derived from the multiplication of the vector V_d by the intricate scaling matrix α

$$A = V_d \times \alpha \tag{5}$$

where, V_d symbolizes the encompassing set of N V_{S21} vectors.

$$A = \begin{bmatrix} S_{img(1,1)} & \cdots & S_{img(1,N)} \\ \vdots & \ddots & \vdots \\ S_{img(N,1)} & \cdots & S_{img(N,N)} \end{bmatrix} \tag{6}$$

where, $S_{img(N,N)}$ signifies individual normalized transmitted data.

The normalized response matrix A subsequently experiences a comprehensive range compression analysis R_{S21}. The range compression process is fundamentally dependent on the range delay $e^{-j2\pi\frac{k}{f_0}t}$, ranging from $(N-1) \times \frac{1}{\lambda}$, where N represents the pixel number, λ represents the wavelength, and the phase shift is denoted by $e^{-j4\pi\frac{f_0}{c}t(j-1)}$. The range compression can be expressed as

$$R_{S21}(m,n) = V_{S21}(m,n).e^{-j2\pi\frac{c}{f_0(m,n)}t}e^{-j4\pi\frac{f_0(m,n)}{c}t(j-1)} \tag{7}$$

Where, m and n represents integer positions in the two-dimensional space and c is the speed of light.

Following the meticulous range compression, the Doppler function delves into calculating the Doppler effect. The Doppler functions are subjected to processing by the velocity vector $v = \{v_i | v_i \in \mathbb{Z}, 5 \geq v_i \geq -5\}$, where v_i represents each elemental component at the index i within the velocity vector v ranging from integer value 5 to -5. The Doppler compensated matrix can be expressed as

$$D_{S21}(m,n) = R_{S21}(m,n)e^{-j4\pi\frac{1}{\lambda}v_i} \tag{8}$$

The apex of this intricate process involves the application of a 2D discrete Fourier transform to the Doppler compensated matrix, operating at frequency indices u and v. The culmination of these operations results in the advanced encryption of the image, embodied by the comprehensive Eq.

$$F_{S21}(m,n) = \sum_{m=1}^{N}\sum_{n=1}^{N} D_{S21}(m,n)e^{-j2\pi\left(\frac{u-m}{N}-\frac{v-n}{N}\right)} \tag{9}$$

Unit cell design

The proposed unit cell of coded metamaterial is presented in Fig. 3(a). The designed structure consists of two different configurations $\varnothing_1$ and $\varnothing_2$ state, corresponding to state 0 and 1, respectively. Silicon material with a dielectric constant of 11.2, an electric conductance of 0.00025 S/m and a conductivity of 2330 Kg/m³ is used to create the coded metamaterial. The metallic constituent is exclusively composed of gold, confirming its identity upon the intricate construct known as a Circular Electric LC structure (CELC). The intrinsic configuration encompasses a circular split ring resonator and a bridging section, denoted as LC, featuring both gapped and without gapped variants to represent the $\varnothing_1$ and $\varnothing_2$ coded state.
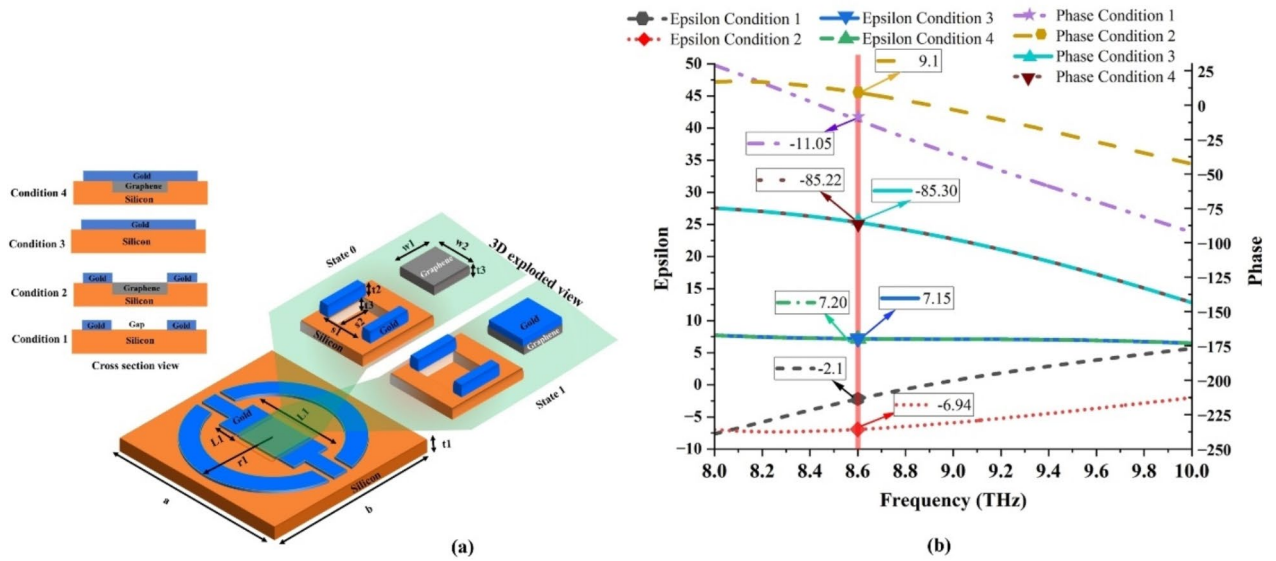
Fig. 3. (**a**) The proposed unit cell design of the coded metamaterial for state 1, state 0, and the four conditions: condition 1, condition 2, condition 3, and condition 4. (**b**) Epsilon and phase distribution of the unit cell for condition 1, condition 2, condition 3, and condition 4.

Specification	Dimension (μm)	Specification	Dimension (μm)
r1	4.4	w1	2.52
L1	4.86	w2	2.16
L2	1.35	s1	2.16
t1	1.30	s2	2.52
t2	0.4	a	9.50
t3	0.4	b	9.50

Table 1. Specification of MC unit cell.

The unit cell structure is depicted in Fig. 3(a), with a substrate dimension $9.50 \times 9.50\ \mu m^2$ and substrate thickness 't1' of $1.30\ \mu m$. The architectural ensemble includes two fundamental constituents: a circular split ring resonator and a cognitively pivotal LC bridge, with the former acting as the principle arbiter of the coded functionality. The outer circular split ring resonator, with a radius r1 of $4.4\ \mu m$, where the radius is symmetrically from the epicenter of the unit cell. The LC bridge, strategically crafted to navigate the binary landscape of digital states 0 ($\varnothing_1$) and 1 ($\varnothing_2$), unfolds its description in Fig. 3 (a) for $\varnothing_1$ and $\varnothing_2$, revealing a precisely drilled rectangular orifice within the substrate. Imposingly, a Graphene entity of congruent dimensions graces the silicon substrate, bearing witness to a hole thickness 't2' and dimensions ('s1' and 's2') of $0.4\ \mu m$, $2.16\ \mu m$ and $2.52\ \mu m$, respectively. Besides, Graphene's own thickness 't3' and dimensions ('w1' and 'w2') echo those of the hole. Notably, the absence of gold metal on the Graphene material during $\varnothing_1$ composes a strategic gap in the LC resonator. Transitioning into $\varnothing_2$, a narrative shift emerges, wherein gold introduces itself onto the Graphene layer, forging a connection within the LC bridge. Here, graphene serves as the intermediary layer sandwiched between the Silicon and gold layers. The extension lengths of the LC bridge denoted as 'L1' ($4.86\ \mu m$) and 'L2' ($1.35\ \mu m$), as exhibited in Fig. 3(a), are important part of encoded material composition. The specification of the MC unit cell is summarized in Table 1.

The designed structure reaches its culmination following an exhaustive analysis of diverse parametric studies, yielding four distinct configurations: condition 1, characterized by Silicon-Gold with a gap in the LC resonator; condition 2, featuring Silicon-Graphene-Gold with a gap in the LC resonator; condition 3, denoted by Silicon-gold without a gap in the LC resonator; and condition 4, defined as Silicon-Graphene-Gold without a gap in the LC resonator. A comprehensive exploration of the epsilon and phase characteristics across conditions 1, 2, 3 and 4 reveals a notable enhancement in structural performance by introducing graphene into the LC gap area, rendering it amenable to coded metamaterial applications. Conditions 1 and 3 lack Graphene inclusion, while conditions 2 and 4 incorporate Graphene within the LC resonator. In the absence of Graphene, the phase difference $\varnothing_1$ and $\varnothing_2$ shows $74°$. With Graphene, this difference expands to $94°$, nearly approaching the critical $90°$ threshold and aligning with the condition $\varnothing_{2^n} = \varnothing_1 + (2^n - 1)\Delta\varnothing \pmod{360}$. The operational frequency is
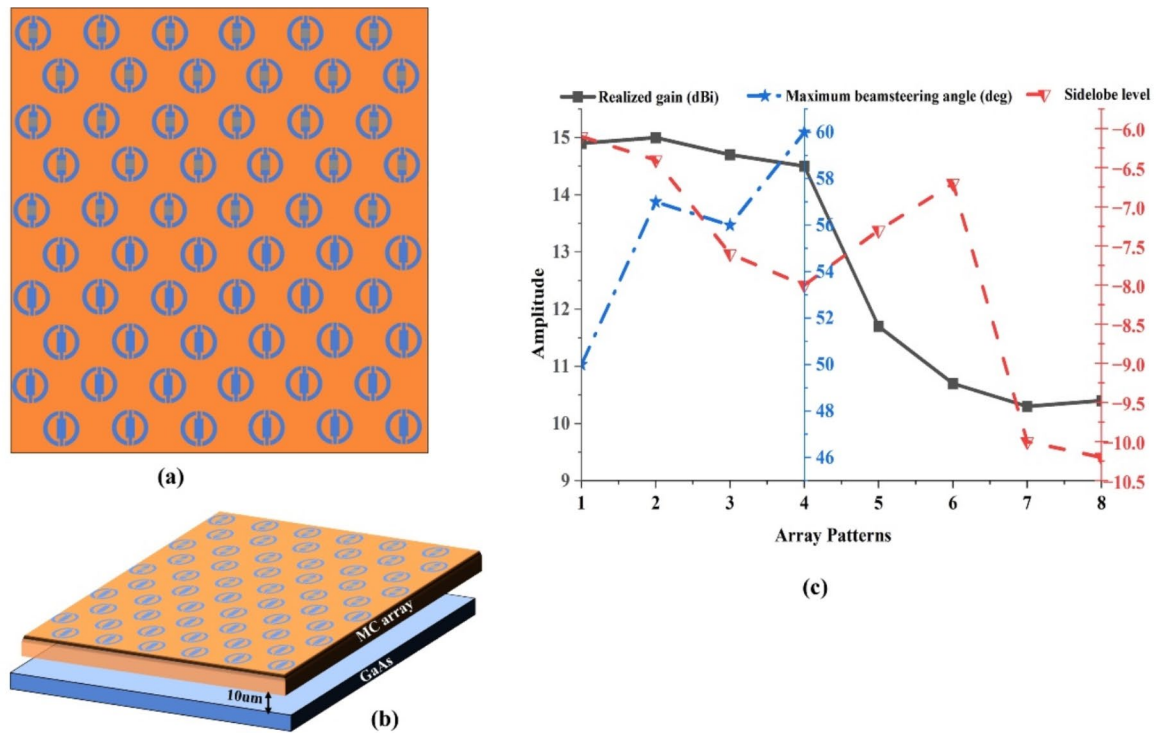
Fig. 4. Array structure (**a**) top, (**b**) perspective view, and (**c**) four array conditions realized gain, maximum beam steering angles and sidelobe level.

Conditions	Epsilon	Phase
1	−2.1	−11.05
2	−6.94	9.1
3	7.15	−85.30
4	7.20	−85.22

Table 2. Summarization of analytical characteristics at 8.6 THz for different structure conditions.

specifically designed at 8.6 THz, at which point the design manifests a distinctive feature. In condition 1, the $\varnothing_1$ structure displays near-zero epsilon metamaterial characteristics, while condition 3 represents the $\varnothing_2$ structure showcasing right-handed metamaterial behavior. Condition 2 features the $\varnothing_1$ structure with epsilon-negative metamaterial traits, whereas in condition 4, for the $\varnothing_2$ structure, it demonstrates right-handed metamaterial characteristics. The epsilon and phase distribution of unit cell for condition 1, condition 2, condition 3 and condition 4 is depicted in Fig. 3(b).

The developed unit cell exhibits focused functionality tailored for $\varnothing_1$ and $\varnothing_2$ states, meticulously designed for beam steering applications at a specific frequency of 8.6 THz. The methodically organized array structure undergoes analysis under four distinct conditions. The finalized developed Array Condition (AC) presents a compelling profile characterized by a low sidelobe and robust beam steering capabilities. Leveraging the two different states $\varnothing_1$ and $\varnothing_2$, the array analysis encompasses four configurations: Silicon-Gold combination (AC1), Silicon-Gold-Air-GaAs combination (AC2), Silicon-Graphene-Gold combination (AC3) and Silicon-Graphene-Gold-Air-GaAs combination (AC4). The amalgamation of four configurations and two design patterns yields a total of eight array patterns. The AC4 top and perspective view is shown in Fig. 4(a) and (b), respectively.

In the context of AC1, the structure comprises two layers of Silicon and Gold. To formulate the AC1 array structure, the arrangement of $\varnothing_1$ and $\varnothing_2$ unit cell states consider the coupling effect, minimizing grating lobes and optimizing beam steering. Consequently, the two states are strategically organized, with half $\varnothing_1$ positioned in the upper portion and the remaining $\varnothing_2$ in the lower portion. The direction of the beam is determined by $\varnothing_1$, resulting in the preparation of two distinct patterns for $+30°$ and $-30°$. The spacing between unit cells within the array is carefully considered to mitigate coupling effects and grating lobe impact. The beamforming results extracted from the analysis are succinctly summarized in Table 2. Each array condition in the table encompasses two patterns, where the odd Pattern signifies $+30°$ and the even Pattern signifies $-30°$. For AC1, Pattern 1 at 8.6 THz demonstrates a gain of 14.9 dBi, although with a higher sidelobe level -6.1 dB and low elevation

beam angle $+24°$. Moving on to AC2, a more complex configuration unfolds with four layers of Silicon-Gold-Air-GaAs arranged for beamforming in a specific direction, introducing an air layer with spacing between MC lens and GaAs material, dimension of $10\mu m$. Meanwhile, AC3 is designed with a three layer composition of Silicon-Graphene-Gold, and AC4 integrates five layers, incorporating Silicon-Graphene-Gold-Air-GaAs for a nuanced combination. Illustrated in Fig. 4(c), the analysis of AC1, AC2, AC3 and AC4 unfolds. In the context of AC2, the structure demonstrates a notable gain of 14.7 dBi, accompanied by an enhanced sidelobe of -7.6 dB and an elevation beam direction of $27°$ for Pattern 3. Pattern 4 achieves a gain of 14.5 dBm, featuring an improved sidelobe of -8 dB and a higher elevation beam direction of $-30°$. Conversely, AC3 reveals superior sidelobe performance compared to AC1 after the integration of Graphene, achieving a sidelobe of -7.3 dB and a beam direction of $27°$ for Pattern 5. For Pattern 6, it demonstrates a sidelobe of -6.7 dB and a beam direction of $-29°$. Through the amalgamation of AC2 and AC3, the final array structure emerges as AC4. AC4 boasts a commendably low sidelobe of -10 dB and a high beam direction of $+30°$ for Pattern 7, whereas, for Pattern 8, it presents a sidelobe of -10.2 dB and a beam direction of $-30°$. The strategic incorporation of a multilayer structure with dielectric material inclusion, to enhance spatial resolution in the Metamaterial Coded lens (MC lens) distantly influences sidelobes and beam steering angles.

Due to the addition of an extra GaAs layer with a higher dielectric constant of 12.94 than the Silicon substrate, the overarching objective of this MC lens is to be employed in beamforming and emerging encryption applications. Image encryption necessitates a high spatial resolution feature, depending on the MC lens wavelength criteria, given by the wavelength equation $\lambda = \frac{c}{f\sqrt{\epsilon}}$. Following the condition $\lambda \propto \frac{1}{\sqrt{\epsilon}}$ from the wavelength equation, the wavelength at 8.6 THz for AC1 is higher than AC4, due to the elevated GaAs dialectic constant in AC4. Nonetheless, spatial resolution is inversely proportional to the wavelength according to the following equation[28]

$$Spatial\ resoluation \propto \frac{D}{\lambda} \tag{10}$$

where, D represents the MC lens aperture size, and λ is the wavelength. According to Eq. (10), a shorter wavelength corresponds to a finer resolution. Consequently, AC4 can effectively enhance spatial resolution compared to the other three AC configurations. The introduction of GaAs into the array structure enhances impedance matching, leading to improved sidelobe and beam steering angles. It is worth noting that the proposed array structures are electrically compact in relation to their wavelength at 8.6 THz.

The performance evaluation of the designed MC lens can be estimated through Performance Metrics (PM), which are determined based on the sidelobe level and maximum beam steering capabilities. The PM is formulated to evaluate the overall system performance by balancing two critical factors: sidelobe level and beam steering range. These parameters are fundamental to the system's effectiveness in applications such as image encryption and security scanning, where sidelobe levels influence spatial resolution and beam steering impacts coverage. The 'Percentage increased PM' is introduced to quantify the improvement achieved when transitioning between different array configurations, highlighting the impact of structural optimizations such as GaAs layer inclusion on sidelobe suppression and beam steering. The PM is expressed by the following equations,

$$PM = (\alpha 1 \times\ sidelobe) + (\beta 1 \times\ beam\ steering) \tag{11}$$

Here, $\alpha 1$ and $\beta 1$ are assigned equal weightage for both sidelobe and maximum beam steering aspects. Utilizing Eq. 11, the performance increase in PM is defined as

$$Percentage\ increased\ (PM) = \frac{PM_{AC_n} - PM_{AC_i}}{PM_{AC_i}} \times\ 100 \tag{12}$$

Here, i represents the initial AC, and n denotes the maximum AC condition. The calculated percentage increase for the four ACs is presented in Table 3. Specifically, the performance increase of AC4 over AC1 is determined to be 19.55%.

Results

The designed MC lens demonstrates the capability to project its beam at both $+30°$ and $-30°$, corresponding to Pattern 1 and Pattern 2, respectively. The three-dimensional radiation pattern for the $+30°$ elevation beam is depicted in Fig. 5(a), while Fig. 5(b) illustrates the radiation pattern for $-30°$ elevation beam. Furthermore, Fig. 5(c) provides a cartesian representation of the radiation pattern in terms of elevation angle. To design the MC lens, CST MWS 2019 is used, where an open boundary condition is applied to extract the results.

The designed MC lens serves the purpose of encrypting an image, as depicted in the presented image encryption scenario in Fig. 6. To execute the image encryption, a 'T' letter is configured on the GaAs substrate frame with the 'T' shape crafted using gold metal. The 'T' shape is discretized into a 5×5 pixel grid. The MC lens is excited by a point source designated as the transmitter (Tx), positioned with a spacing of $80\mu m$. A point receiver (Rx) is employed to collect the transmitted data S21. Image encryption involves two approaches for collecting S21 data. The first involves a fixed beam in a desired direction, while the second involves a fixed object capable of scanning the beam with predetermined beam steering. Due to the broader 3dB angular beamwidth, the second option is excluded from consideration for encryption. Consequently, during the collection of image encryption data, the object is moved along its $+x$-axis from 0 to 100 points with an interval of 25 and along its $-y$-axis from 0 to 100 points with a 25 points interval. This movement yields a 5×5 matrix comprising 25 S21 data sets. Subsequently, these 25 S21 data sets are processed by subtracting the data obtained without the

Array conditions		Frequency (THz)	Realized gain (dBm)	Sidelobe level (dB)	Beam steering	Maximum beam steering	Percentage increased (PM)
AC 1	Pattern 1	8.6	14.9	−6.1	24	50	0%
	Pattern 2		15	−6.4	−26		
AC 2	Pattern 3		14.7	−7.6	27	57	8.38%
	Pattern 4		14.5	−8	−30		
AC 3	Pattern 5		11.7	−7.3	27	56	8.94%
	Pattern 6		10.9	−6.7	−29		
AC 4	Pattern 7		10.3	−10.0	30	60	19.55%
	Pattern 8		10.4	−10.2	−30		

Table 3. Performance analysis of the proposed MC lens.
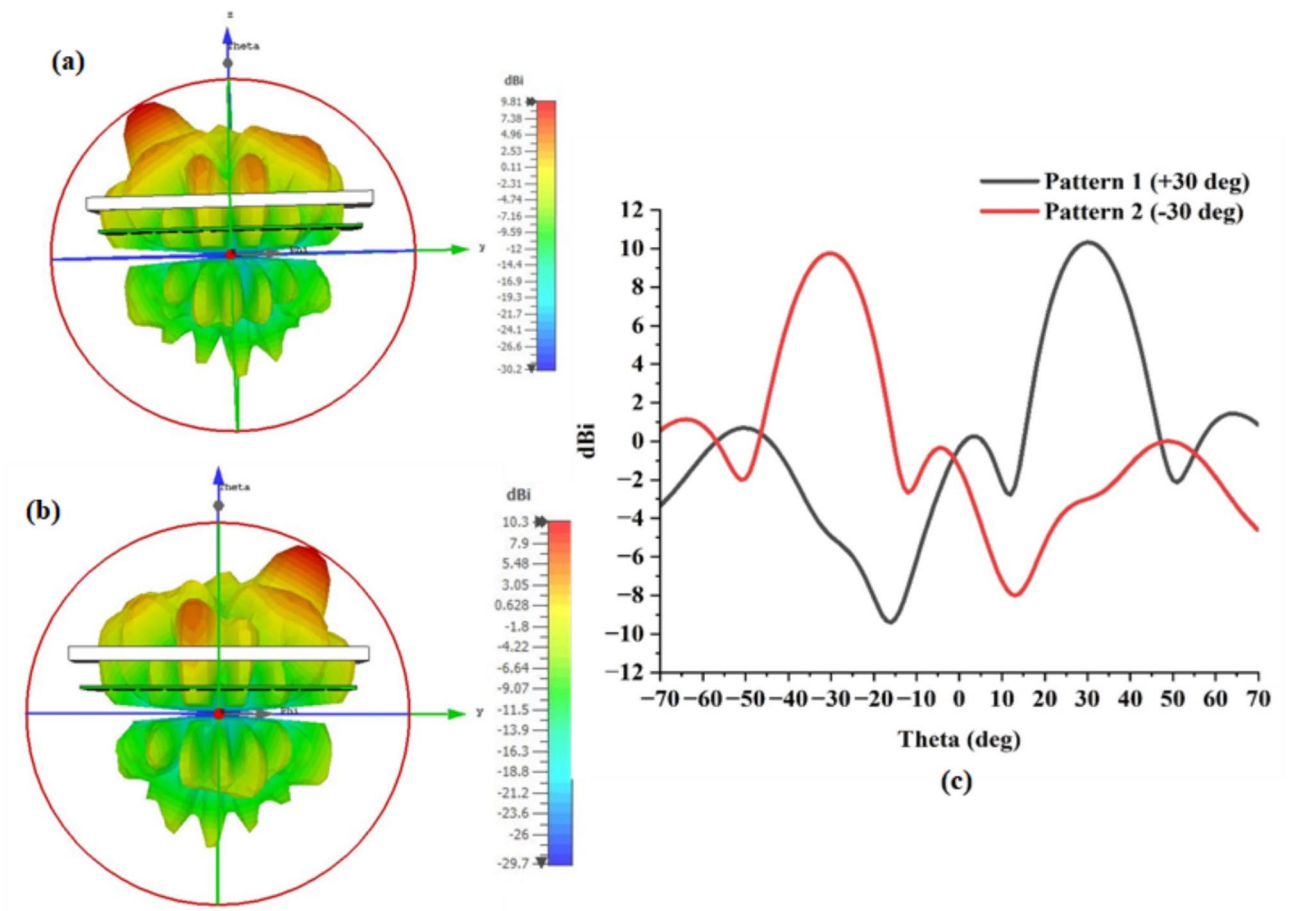
Fig. 5. 3D radiation pattern for (**a**) $+30°$, (**b**) $-30°$ and (**c**) Cartesian representation of elevation beam steering at 8.6 THz.

object for the 8−8.5 THz frequency bandwidth. The collected data is then normalized by using Eqs. 4–6. The normalized data undergoes further processing using Eqs. 7 and 8. Finally, employing a 2D FFT, the processed data is encrypted to yield the image output using MATLAB 2023a, as illustrated in Fig. 6.

Comparison and future work

Various coding metamaterials have been developed for terahertz beam steering and imaging applications. Lin et al. explored metamaterial with optical activation using phase-change materials like GeTe, achieving beam steering at 0°, 30°, and 40°. However, traditional active metamaterial often require semiconductor-based controlling elements, which can be challenging to implement in high-frequency terahertz applications[29]. Liu et al. proposed programmable coding metasurfaces, achieving up to 30° beam steering, but phase mismatches due to sub-array coupling impacted sidelobe performance[26]. Similarly, Giovampaola and Engheta introduced
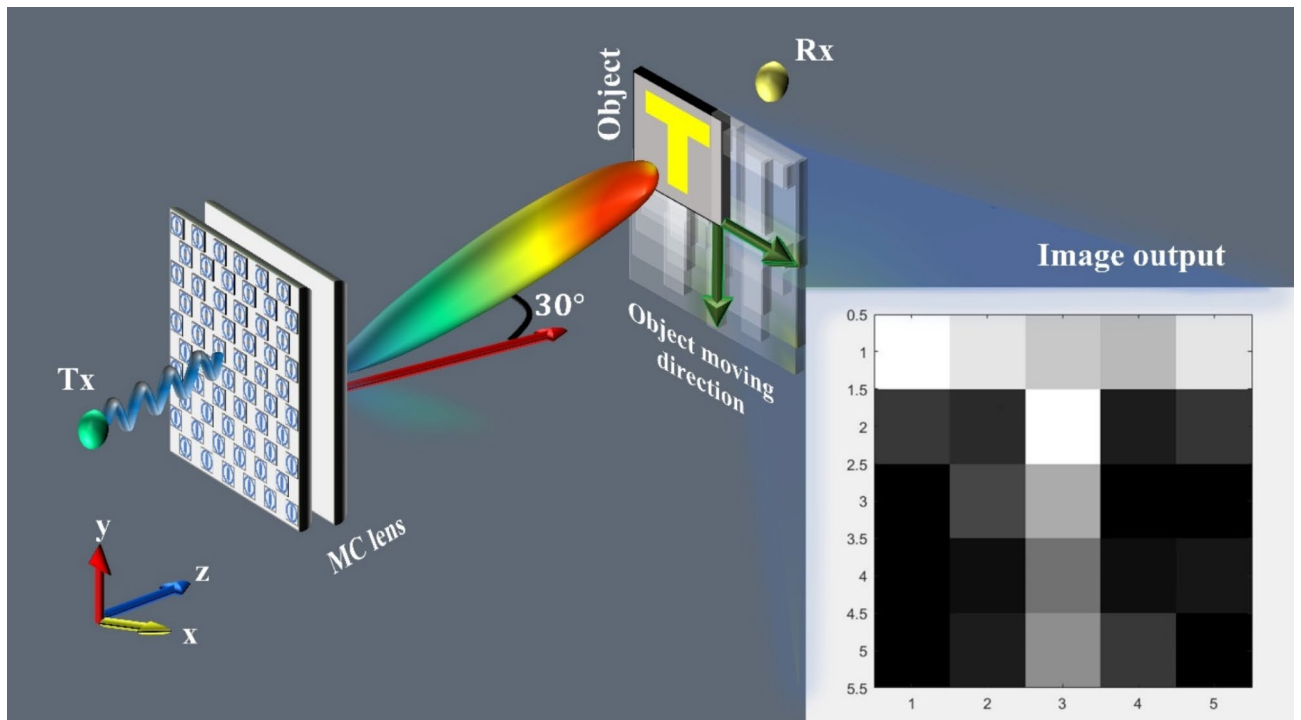
Fig. 6. Analytical setup of encryption image data.

digital metamaterials for ENZ (negative epsilon zero) tunneling at 740.23 THz, but bandwidth limitations and dispersion of the negative-permittivity bit posed challenges[22]. Seyed Ehsan Hosseininejad et al. developed a graphene-based metasurface for terahertz imaging, focusing on adaptive focal points[30]. Meanwhile, Farzin et al. designed a coded metasurface for THz wavefront control, achieving sidelobe levels of −19 dB[31]. In contrast to existing methodologies, this research introduces an innovative approach with the development of a 1-bit Coded Metamaterial Array specifically engineered for terahertz frequencies at 8.6 THz. The array demonstrates advanced beam steering capabilities by precisely manipulating the phase difference and epsilon shifting within the metamaterial unit cells. Distinctive features of this design include a high-precision phase manipulation mechanism that enables efficient beam steering within a range of $\pm 30°$, along with superior sidelobe suppression, achieving a sidelobe level of −10.4 dBm. These characteristics enhance the metamaterial's ability to operate in terahertz encryption and imaging applications with high spatial resolution and improved security. The proposed structure offers scalable deployment potential, allowing for efficient use in a variety of terahertz-based systems, including encryption protocols, advanced imaging systems, and secure communications.

As part of ongoing efforts to advance this research, future work will focus on the fabrication and experimental validation of the proposed metamaterial design. The first step in the fabrication process will involve constructing the 5×5 pixel unit cells using advanced photolithography techniques to create the required phase and epsilon-shifting materials pattern. By incorporating graphene or Gallium Arsenide (GaAs) with a tuneable permittivity, the goal is to precisely control the phase shifts and enable reconfigurability at terahertz frequencies. The fabrication process will also integrate transistor arrays for dynamic control of the phase and epsilon shifts within the unit cells. This approach will enable experimental validation of the proposed encryption capabilities and beam steering performance. Additionally, the future fabrication plan includes testing in a controlled environment to assess the metamaterial's efficiency in real-world applications, including terahertz imaging and wireless communication. These experimental results are expected to provide valuable insights for further optimization of the design and its adaptation for commercial terahertz applications.

Conclusion

The novel multilayer coded metamaterial is tailored for digital encryption, operating at a single frequency of 8.6 THz. The uniqueness of the design technique lies in the combination of phase difference and meticulous epsilon shifting. This design approach renders the coded multilayer more sophisticated, resulting in a noteworthy reduction of the sidelobe level to a maximum of −9 dB. Additionally, it enhances the flexibility of its beam steering angle, reaching a maximum of $60°$. The strategic inclusion of GaAs in the MC lens composition enhances the special resolution of the structure, thereby contributing to the heightened performance metrics of 19.55%. Specifically, the performance metrics exhibit substantial improvement, underscoring the positive impact of GaAs inclusion on the MC lens. The practical application of the MC lens extends to the encryption of a 'T' shaped image in a specific elevation direction, precisely at $+30°$. This encryption process is achieved through the synergistic application of range compression, Doppler processing and 2D FFT. Beyond its primary function

in digital encryption, the designed metamaterial lens also demonstrates the suitability for various applications such as superlensing, image scanning, conveyor systems and modern security purposes.

Data availability

The datasets used and/or analysed during the current study available from the corresponding author on reasonable request.

References

1. Luk, K. M. et al. A microfabricated low-profile wideband antenna array for terahertz communications. *Sci. Rep.* **7** (1), 1268 (2017).
2. Pengnoo, M. et al. Digital twin for metasurface reflector management in 6G terahertz communications. *IEEE Access.* **8**, 114580–114596 (2020).
3. Shlezinger, N., Alexandropoulos, G. C., Imani, M. F., Eldar, Y. C. & Smith, D. R. Dynamic metasurface antennas for 6G extreme massive MIMO communications. *IEEE Wirel. Commun.* **28** (2), 106–113 (2021).
4. Sahu, T. K. et al. Free-standing 2D gallium nitride for electronic, excitonic, spintronic, piezoelectric, thermoplastic, and 6G wireless communication applications. *NPG Asia Mater.* **15** (1), 49 (2023).
5. Dash, S., Psomas, C., Patnaik, A. & Krikidis, I. An ultra-wideband orthogonal-beam directional graphene-based antenna for THz wireless systems. *Sci. Rep.* **12** (1), 22145 (2022).
6. Álvarez-Sanchis, J., Vidal, B., Tretyakov, S. & Díaz-Rubio, A. Loss-induced performance limits of all-dielectric metasurfaces for terahertz sensing. *Phys. Rev. Appl.* **19** (1), 014009 (2023).
7. Tian, X. et al. Dynamically switchable tri-functional THz-integrated metamaterial absorber based on VO2-graphene. *Opt. Laser Technol.* **165**, 109609 (2023).
8. Amarasinghe, Y. et al. Broadband wide-angle terahertz antenna based on the application of transformation optics to a Luneburg lens. *Sci. Rep.* **11** (1), 5230 (2021).
9. Mashayekhi, M., Kabiri, P., Nooramin, A. S. & Soleimani, M. A reconfigurable graphene patch antenna inverse design at terahertz frequencies. *Sci. Rep.* **13** (1), 8369 (2023).
10. Cui, T. J., Qi, M. Q., Wan, X., Zhao, J. & Cheng, Q. Coding metamaterials, digital metamaterials and programmable metamaterials. *Light: Sci. Appl.*, **3**, 10, pp. (2014). e218-e218.
11. Degl'Innocenti, R., Lin, H. & Navarro-Cía, M. Recent progress in terahertz metamaterial modulators, *Nanophotonics*, vol. 11, no. 8, pp. 1485–1514, (2022).
12. Sun, J. et al. A flexible U-shaped metamaterial terahertz quarter-wave plate with corner design. *Opt. Laser Technol.* **175**, 110834 (2024).
13. Gao, L. H. et al. Broadband diffusion of terahertz waves by multi-bit coding metasurfaces. *Light: Sci. Appl.*, **4**, 9, pp. (2015). e324-e324.
14. Dai, J. Y., Zhao, J., Cheng, Q. & Cui, T. J. Independent control of harmonic amplitudes and phases via a time-domain digital coding metasurface. *Light: Sci. Appl.* **7** (1), 90 (2018).
15. Xu, J., Liu, W. & Song, Z. Terahertz dynamic beam steering based on graphene coding metasurfaces. *IEEE Photonics J.* **13** (4), 1–9 (2021).
16. Ansari, M., Zhu, H., Shariati, N. & Guo, Y. J. Compact planar beamforming array with endfire radiating elements for 5G applications. *IEEE Trans. Antennas Propag.* **67** (11), 6859–6869 (2019).
17. Ullah, M., Keshavarz, R., Abolhasan, M., Lipman, J. & Shariati, N. Multi-service Compact Pixelated Stacked Antenna with different pixel shapes for IoT Applications. *IEEE Internet Things J.*, (2023).
18. Keshavarz, R., Shariati, N. & Miri, M. A. Real-time Discrete Fractional Fourier transform using Metamaterial coupled Lines Network. *IEEE Trans. Microwave Theory Tech.*, (2023).
19. Keshavarz, R., Majidi, E., Raza, A. & Shariati, N. Ultra-fast and efficient design method using Deep Learning for Capacitive Coupling WPT System. *IEEE Trans. Power Electron.*, (2023).
20. Taghvaee, H., Liu, F., Díaz-Rubio, A. & Tretyakov, S. Perfect-Lens Theory enables Metasurface Reflectors for Subwavelength focusing. *Phys. Rev. Appl.* **19** (1), 014004 (2023).
21. Tirole, R. et al. Saturable time-varying mirror based on an epsilon-near-zero material. *Phys. Rev. Appl.* **18** (5), 054067 (2022).
22. Della Giovampaola, C. & Engheta, N. Digital metamaterials. *Nat. Mater.* **13** (12), 1115–1121 (2014).
23. Liu, T., Han, Z., Duan, J. & Xiao, S. Phase-change metasurfaces for dynamic image display and information encryption. *Phys. Rev. Appl.* **18** (4), 044078 (2022).
24. Liang, L. et al. Anomalous terahertz reflection and scattering by flexible and conformal coding metamaterials. *Adv. Opt. Mater.* **3** (10), 1374–1380 (2015).
25. Suzuki, T. & Kondoh, S. Negative refractive index metasurface in the 2.0-THz band. *Opt. Mater. Express.* **8** (7), 1916–1925 (2018).
26. Liu, C. X. et al. Programmable manipulations of terahertz beams by transmissive digital coding metasurfaces based on liquid crystals. *Adv. Opt. Mater.* **9** (22), 2100932 (2021).
27. Ahamed, E., Keshavarz, R., Franklin, D. & Shariati, N. Software-defined programmable Metamaterial Lens System for dynamic Wireless power transfer applications. *IEEE Trans. Antennas Propag.*, (2024).
28. Zhu, W. et al. Super-resolution ultrasonic Lamb wave imaging based on sign coherence factor and total focusing method. *Mech. Syst. Signal Process.* **190**, 110121 (2023).
29. Lin, Q., Wong, H., Huitema, L. & Crunteanu, A. Coding metasurfaces with reconfiguration capabilities based on optical activation of phase-change materials for terahertz beam manipulations. *Adv. Opt. Mater.* **10** (1), 2101699 (2022).
30. Hosseininejad, S. E. et al. Reprogrammable graphene-based metasurface mirror with adaptive focal point for THz imaging. *Sci. Rep.* **9** (1), 2868 (2019).
31. Farzin, P., Nooramin, A. S. & Soleimani, M. Reprogrammable reflection-transmission integrated coding metasurface for real-time terahertz wavefront manipulations in full-space. *Sci. Rep.* **14** (1), 11156 (2024).

Author contributions

Eistiak Ahamed: Conceptualization, Methodology, Validation, Software, Data curation, Writing- Original draft preparation. Rasool Keshavarz: Conceptualization, Methodology, Visualization, Investigation. Negin Shariati: Supervision, Investigation, Writing- Reviewing and Editing.

Declarations

Competing interests
The authors declare no competing interests.

Additional information
Correspondence and requests for materials should be addressed to E.A.

Reprints and permissions information is available at www.nature.com/reprints.

Publisher's note Springer Nature remains neutral with regard to jurisdictional claims in published maps and institutional affiliations.